Eur. Phys. J. Spec. Top.
https://doi.org/10.1140/epjs/s11734-025-01652-6

THE EUROPEAN PHYSICAL JOURNAL SPECIAL TOPICS

Regular Article

Complex synchronization in memristor-coupled Chialvo Neurons

Lili Wang[1], Hao Gao[1,2], Chunbiao Li[2,3,a], Qianyuan Tang[4], and Dante Chialvo[4,5]

[1] School of Electronic and Information Engineering, Anhui Jianzhu University, Hefei 230009, Anhui, China
[2] School of Artificial Intelligence, Nanjing University of Information Science & Technology, Nanjing 210044, Jiangsu, China
[3] School of Electronic & Information Engineering, Nanjing University of Information Science & Technology, Nanjing 210044, Jiangsu, China
[4] Department of Physics, Hong Kong Baptist University, Hong Kong 999077, China
[5] Center for Complex Systems & Brain Sciences (CEMSC3), Universidad Nacional de San Martín, Buenos Aires, Argentina

Received 11 February 2025 / Accepted 24 April 2025
© The Author(s), under exclusive licence to EDP Sciences, Springer-Verlag GmbH Germany, part of Springer Nature 2025

Abstract The study of neurons and their interaction mechanisms plays a critical role in advancing our understanding of brain functionality and neural network dynamics. Recent studies demonstrated that memristor-based neural networks can effectively simulate biological neural behaviors and exhibit rich dynamical properties. In this paper, we propose a tanh-type memristor-coupled Chialvo neuron model and investigate its dynamic behaviors and synchronization patterns under varying parameter conditions. We demonstrate that fine-tuning the external excitation current can effectively regulate the synchronization state between neurons, highlighting the potential of memristors in controlling neural network synchronization. Using the Hilbert transform, we construct analytic signals to extract the instantaneous phase spectra of the membrane potentials of two coupled neurons. The phase difference is calculated by subtracting the instantaneous phases, and a synchronization coefficient is introduced to quantify the degree of synchronization. Finally, the validity of our findings is confirmed through experimental implementation on a CH32 microcontroller.

1 Introduction

Deciphering the brain's information processing mechanisms remains a grand challenge in contemporary neuroscience, driven by the interplay of its structural complexity, dynamic adaptability, and emergent functional properties [1–4]. Advances in nonlinear dynamics [5, 6], have provided revolutionary insights into neural systems by formalizing critical phenomena such as bifurcations, chaos, and multistability. Nonlinear systems, circuits and neurons exhibit rich dynamics, which facilitate encoding, transmission, and multiscale integration of information for physical world [7]. Of particular significance is synchronization, a self-organized process where neurons adjust their firing rhythms to achieve temporal coordination [8]. This phenomenon underpins critical functions ranging from sensory integration and perceptual binding to memory formation and consciousness [9, 10], establishing itself as a fundamental mechanism in neural information processing.

The complexity of neural dynamics presents significant modeling challenges: biological neurons operate in noisy, high-dimensional environments with adaptive synaptic connections, rendering traditional continuous models computationally intractable for large-scale simulations [11–13]. While multiple simplified models have been proposed, the Chialvo neuron model [14] stands out for its elegant balance of computational efficiency and dynamical richness. Originally developed to capture fundamental neuronal firing patterns [15], this discrete model has proven particularly valuable for investigating synchronization and chaos in neural systems [16], though it still faces limitations in representing synaptic plasticity and adaptive connectivity-hallmark features of biological neural networks.

Against this backdrop, the memristor [17], as a novel memory element, emerges as a promising solution for addressing these limitations through its capability to simulate synaptic behavior via nonlinear resistance and memory functions. Memristors can not only simulate the weighting and plasticity of individual synapses [18] but

[a] e-mail: goontry@126.com (corresponding author)

also imitate complex information processing mechanisms within neurons [19]. Yang et al. proposed that a magnetic flux-controlled memristor (MFCM) be connected to a FitzHugh-Nagumo (FHN) neural circuit to construct a memristive circuit, and its equivalent memristive neuron is capable of perceiving modulation from an external magnetic field [20]. Zhang et al. proposed that six modes of offset boosting are triggered in the neuronal model by varying the electric field coupling coefficients [21]. While these studies predominantly focused on continuous memristors [22], discrete memristors [23], despite their potential stability advantages, remain relatively unexplored. Recently, two Chialvo neurons are coupled by a memristor for observing the various synchronization behaviors [24], where phase synchronization and complete synchronization have been obtained under different coupling gains. Therefore, all the synchronizations are based on the memristor gains while the influence of external stimulation in synchronization remains unexplored. In this work, a new tanh-type discrete memristor is introduced for coupling two Chialvo neurons, aiming to achieve enhanced control over the neural synchronization patterns. Furthermore, the influence of external stimulus current to synchronization in Chialvo neurons are investigated rather than from the view of memristor coupling. Note that, Hilbert transform-based phase extraction is employed here to characterize the modes of synchronization rather than the conventional difference-based methods.

The novelty and main contributions of this work are summarized as follows:

1 A tanh-type memristor-coupled Chialvo neuron is proposed, and its chaotic characteristics are analyzed [25, 26]. By varying the external stimulation current, the synchronization state of the membrane potential under changing external conditions is investigated.
2 Using the Chialvo neuron coupling system established in this paper, an offset boosting [27] and local amplitude control mechanism [28] are designed to show the system's impressive adjustable properties.
3 The CH32-based circuit implementation is used to verify the offset boosting and local amplitude control of the proposed neuron coupling system. The asynchronous to synchronous state of membrane potential is clearly displayed on the oscilloscope.

The remainder of this article is organized as follows. In Sect. 2, the MCC neuron is constructed and analyzed using Lyapunov exponents, revealing its typical oscillatory states. Section 3 explores synchronization behaviors in the MCC neuron through the application of the Hilbert transform. In Sect. 4, a nonbifurcation parameter for offset boosting is extracted, and local amplitude control is identified. Section 5 presents the hardware implementation of the proposed model. Finally, Sect. 6 concludes the article by summarizing the key findings and contributions.

2 Basic dynamics of the MCC neuron

2.1 Discrete memristor model

In this work, we introduce a discrete memristor-based coupling mechanism between Chialvo neurons. Discrete memristors, with their quantized resistance, offer enhanced stability, digital compatibility, lower power consumption, improved scalability, simplified programming, neuromorphic advantages, and extended endurance, making them ideal for next-generation memory and energy-efficient neuromorphic computing. The mathematical model of the discrete tanh-type memristor is given as follows:

$$\begin{cases} i_n = W(\varphi_n)v_n = \tanh(\varphi_n)v_n \\ \varphi_{n+1} = \varphi_n + v_n \end{cases} \tag{1}$$

where the magnetic flux is represented by φ_n, and the input voltage of the memristor is defined as $v_n = A\sin(\omega_n)$. In the MATLAB simulation environment, we fix the frequency $\omega = 0.1$, the initial magnetic flux $\varphi_0 = 0.1$, and set different amplitudes as $A = 0.05$, $A = 0.10$, and $A = 0.15$. The resulting amplitude-related hysteresis loops of the discrete memristor are shown in Fig. 1a. Moreover, by fixing $A = 0.1$, $\varphi_0 = 0.1$, and using different frequencies $\omega = 0.1$, $\omega = 0.3$, and $\omega = 0.5$, the frequency-dependent hysteresis loops of the memristor are shown in Fig. 1b. The numerical results in Fig. 1 can perfectly display the elegant pinched hysteresis loops at the origin.

2.2 MCC Neuron Architecture

Using the tanh-type memristor model described in the previous section, we couple two Chialvo neurons (denoted as C_1 and C_2), constructing the memristor-coupled Chialvo (MCC) neuron [29, 30]. The model structure is illustrated in Fig. 2.

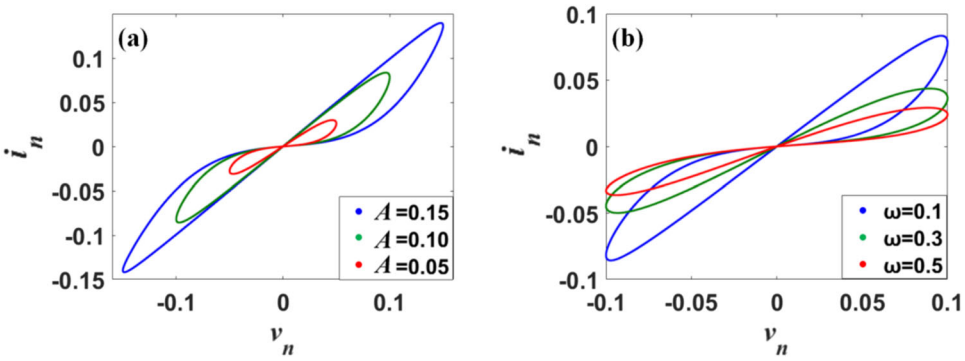


Fig. 1 Fingerprints of the discrete memristor with $\varphi_0 = 0.1$: **a** amplitude-related pinched hysteresis loops when $\omega = 0.1$ and $A = 0.05$, $A = 0.10$, $A = 0.15$, **b** frequency-related pinched hysteresis loops when $A = 0.1$ and $\omega = 0.1$, $\omega = 0.3$, $\omega = 0.5$

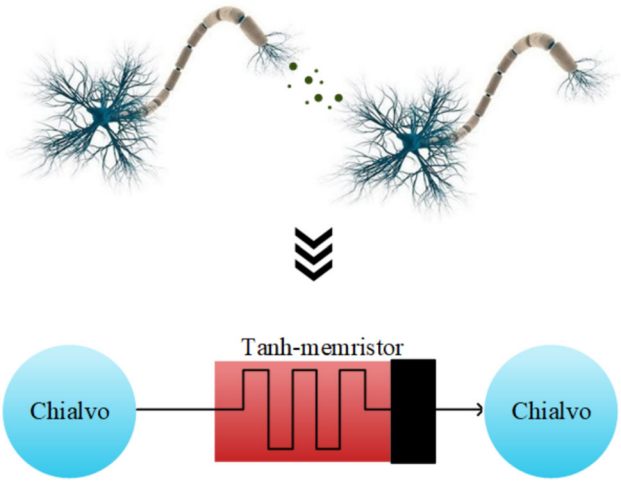


Fig. 2 Topology of the MCC neuron

The five-dimensional MCC neuron model is defined as:

$$\begin{cases} x_1(n+1) = x_1^2(n)e^{(y_1(n)-x_1(n))} + I_1 + k(x_1(n) - x_2(n))\tanh(\varphi(n)) \\ y_1(n+1) = ay_1(n) - bx_1(n) + c \\ \varphi(n+1) = \varphi(n) - 0.1(x_1(n) - x_2(n)) \\ x_2(n+1) = x_2^2(n)e^{(y_2(n)-x_2(n))} + I_2 + k(x_2(n) - x_1(n))\tanh(\varphi(n)) \\ y_2(n+1) = ay_2(n) - bx_2(n) + c \end{cases} \tag{2}$$

Here, x_1 and x_2 represent the membrane potentials of the Chialvo neurons, y_1 and y_2 are the recovery variables, I_1 and I_2 are the external excitation currents. The parameter k denotes the memristor coupling strength, while n refers to the number of iterations in the mapping process. Consistent with primitive neurons, here we select $a = 0.89$, $b = 0.18$, $c = 0.28$. And the external stimulus current I_1, I_2 and coupling coefficient are set for rich dynamics.

2.3 Fixed point analysis of the MCC neuron

The stability of these fixed points can be characterized by the eigenvalues of the Jacobian matrix of the mapping at the equilibrium point [31]. The Jacobian matrix of the MCC neuron is given by:

$$J = \begin{bmatrix} A & x_1^2 e^{(y_1-x_1)} & k(x_1 - x_2)\sec^2(\varphi) & -k\tanh(\varphi) & 0 \\ -b & a & 0 & 0 & 0 \\ -0.1 & 0 & 1 & 0.1 & 0 \\ -k\tanh(\varphi) & 0 & k(x_2 - x_1)\sec^2(\varphi) & B & x_2^2 e^{(y_2-x_2)} \\ 0 & 0 & 0 & -b & a \end{bmatrix} \tag{3}$$

$$A = 2x_1 e^{(y_1-x_1)} - x_1^2 e^{(y_1-x_1)} + k\tanh(\varphi) \tag{4}$$

Table 1 Solutions of eigenvalue equation (Eq. 9) with $a = 0.89$, $b = 0.18$, $c = 0.28$, $I_1 = 0.03$, $I_2 = 0.04$ and $k = 0.15$, $k = 0.17$

	λ_1	λ_2	λ_3	λ_4	λ_5
$k = 0.15$	− 1.0193	0.9932 + 0.4602i	0.9332–0.4606i	1.0907	0.9982
$k = 0.17$	− 1.2737	0.9462 + 0.4113i	0.9462–0.4113i	0.9340	1.0442

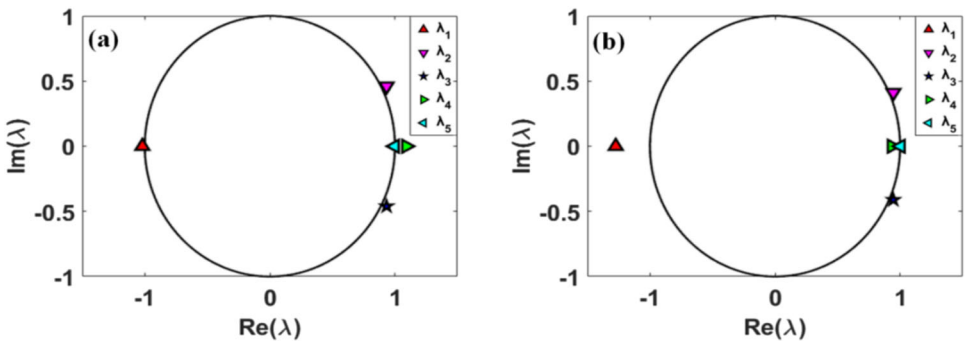


Fig. 3 The loci of two sets of eigenvalues in the complex plane with varying coupling strength k: **a** $k = 0.15$. **b** $k = 0.17$. Other initial conditions and parameters: $(x_1(0), y_1(0), \varphi(0), x_2(0), y_2(0)) = (0.5, 0.1, 0.1, 0.5, 0.1)$, $a = 0.89$, $b = 0.18$, $c = 0.28$, $I_1 = 0.03$, and $I_2 = 0.04$

$$B = 2x_2 e^{(y_2 - x_2)} - x_2^2 e^{(y_2 - x_2)} + k\tanh(\varphi) \tag{5}$$

The characteristic equation for the eigenvalues of the Jacobian matrix is expressed as:

$$(\lambda e - J) = \begin{bmatrix} C & -x_1^2 e^{(y_1 - x_1)} & -k(x_1 - x_2)\mathrm{sech}^2(\varphi) & k\tanh(\varphi) & 0 \\ b & \lambda - a & 0 & 0 & 0 \\ 0.1 & 0 & \lambda - 1 & -0.1 & 0 \\ k\tanh(\varphi) & 0 & -k(x_2 - x_1)\mathrm{sech}^2(\varphi) & D & -x_2^2 e^{(y_2 - x_2)} \\ 0 & 0 & 0 & b & \lambda - a \end{bmatrix} \tag{6}$$

$$C = \lambda - 2x_1 e^{(y_1 - x_1)} - x_1^2 e^{(y_1 - x_1)} + k\tanh(\varphi) \tag{7}$$

$$D = \lambda - 2x_2 e^{(y_2 - x_2)} - x_2^2 e^{(y_2 - x_2)} + k\tanh(\varphi) \tag{8}$$

The eigenvalues of the Jacobian matrix can be calculated from the following equation:

$$\det(\lambda e - J) = 0 \tag{9}$$

Set $a = 0.89$, $b = 0.18$, $c = 0.28$, $I_1 = 0.03$, $I_2 = 0.04$ and using coupling strengths $k = 0.15$ and $k = 0.17$, the five equilibrium points are computed, and their eigenvalues are shown in Table 1. These eigenvalues are plotted on the complex plane (as shown in Fig. 3) with a unit circle provided for reference. Obviously, since $\lambda_5 > 1$, so the points when $k = 0.15$ and $k = 0.17$ are unstable.

2.4 Lyapunov exponents of the MCC neuron

Next, let us examine dual parameter variations of the MCC neuron as described in Eq. (2). From the Lyapunov exponents under these dual variations, as shown in Fig. 4, we observe significant chaotic behavior within the parameter ranges $I_1 = \{m \text{ — } 0.03 < m < 0.05\}$ and $I_2 = \{m \text{ — } 0.03 < m < 0.05\}$. The Lyapunov exponents LE_1, LE_2, and LE_3 exhibit positive values to varying degrees. The results indicate that the system primarily exists in a hyper-chaotic state across these parameters. Since LE_4 are negative and LE_5 is less than LE_4, so the LE_5 is ignored in the Fig. 4. These chaotic dynamics can significantly affect the dynamic behavior and information transmission within the neural network, highlighting the need for further investigation.

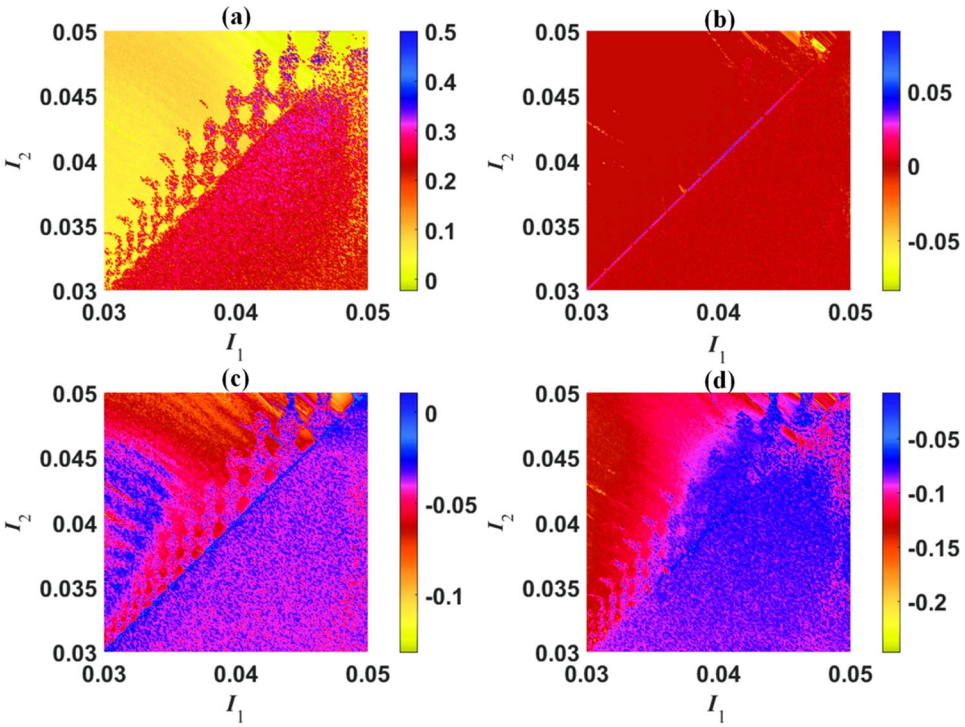


Fig. 4 Mixed 2-D Lyapunov exponents with the initial value $(x_1(0), y_1(0), \varphi(0), x_2(0), y_2(0)) = (0.5, 0.1, 0.1, 0.5, 0.1)$, $a = 0.89$, $b = 0.18$, $c = 0.28$, $k = 0.17$, $I_1 = \{m — 0.03 < m < 0.05\}$ and $I_2 = \{m — 0.03 < m < 0.05\}$

2.5 Typical oscillatory states in the MCC neuron

In previous subsections, we examined the neuron model's behavior using consistent initial firing states. Now we will investigate how varying external stimuli affect the neurons'membrane potentials. When $(I_1, I_2) = (0.03, -0.02)$, as shown in Fig. 5a, the membrane potentials of the neurons remain at rest. In this state, the neurons are in a stable resting condition, ready to respond to external stimuli. As the external stimulus increases, when $(I_1, I_2) = (0.05, 0.01)$, the neurons transition to a bursting state, as shown in Fig. 5b. This state represents a rapid

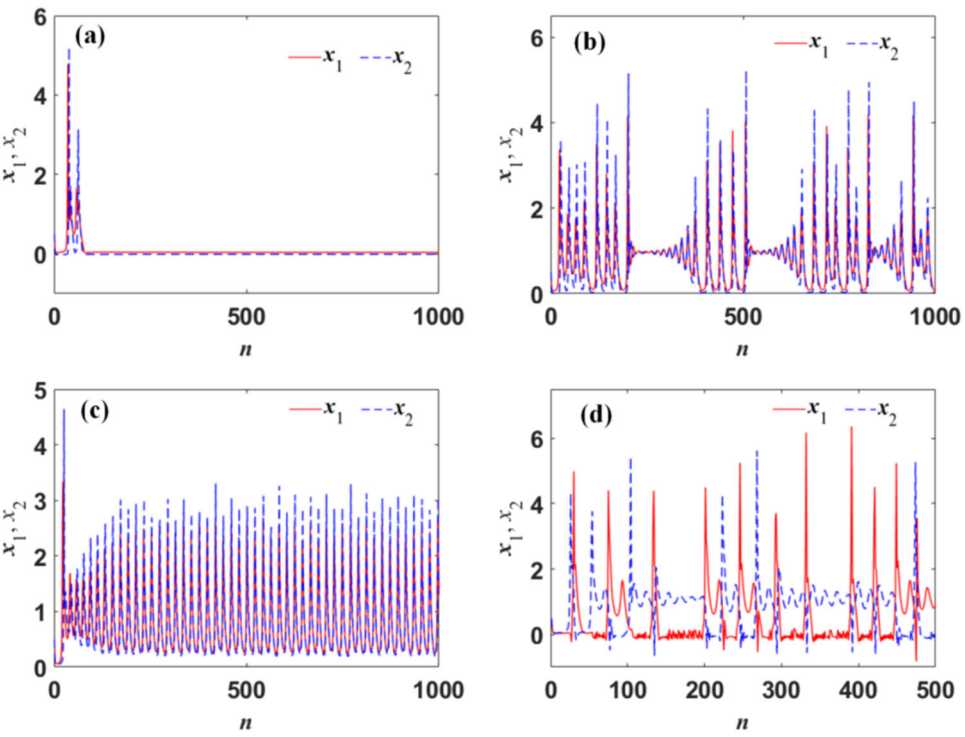


Fig. 5 Membrane potentials: **a** quiescent neurons. **b** spiking and bursting neurons. **c** Bursting and spiking neurons. **d** reverse spiking and bursting neurons

response to strong stimuli, characterized by a sharp change in membrane potential and significant firing activity. Further increasing the external stimulus to $(I_1, I_2) = (0.05, 0.04)$ results in the membrane potential entering a spiking state, as shown in Fig. 5c. This indicates a high sensitivity to the specific type of stimulus, where the membrane potential exhibits high-frequency and high-amplitude spiking behavior. Additionally, when $(I_1, I_2) = (0.041, 0.04)$, an alternating pattern where one neuron fires while the other is inhibited are observed, as shown in Fig. 5d. This reverse spiking mode reflects the interaction between neurons and may be related to dynamic regulation within the neural network.

3 Synchronization behavior in the MCC Neuron

3.1 Phase synchronization based on the Hilbert transform

Building on our analysis of oscillatory states in the MCC neuron, we next examined the synchronization properties between coupled neurons using the Hilbert transform method and synchronization coefficients. Our results demonstrate that precise modulation of coupling strength and external excitation current can drive paired neurons from asynchronous firing to complete synchronization. This finding reveals how memristor-based coupling can effectively regulate neural synchronization, contributing to our understanding of synchronization mechanisms in brain networks.

The Hilbert transform is a signal processing tool commonly used to extract the instantaneous characteristics of a signal, particularly its phase information. In signal analysis, the instantaneous phase and frequency of a signal can be determined by constructing an analytic signal from the Hilbert transform. This method, originally proposed by Gabor, converts a time-domain signal into a complex function of time, providing both phase and amplitude information. The analytic signal is defined as:

$$\zeta_1(n) = s(n) + is_H(n) = A(n)e^{i\phi(n)} \tag{10}$$

where $s_H(n)$ is the Hilbert transform of $s(n)$:

$$s_H(n) = \int_{-\infty}^{\infty} \frac{s(\tau)}{\pi(n-\tau)} d\tau = s(n) * \frac{1}{\pi n} \tag{11}$$

The instantaneous amplitude $A(n)$ and phase $\phi(n)$ of the signal can then be uniquely determined. The angle function represents the angle between the complex number in the complex plane and the real axis. For a complex number $z = a + bi$, where a is the real part and b is the imaginary part, the argument θ (angle measured counterclockwise from the positive real axis to complex number z) can be computed as:

$$\theta = \text{at}an2(b, a) \tag{12}$$

Here, 'atan2' is the two-argument arctangent function. It resolves the ambiguity that may arise when dividing sine by cosine, ensuring the correct quadrant of the angle. The phase difference between the two signals is calculated as:

$$\Delta\phi(n) = \phi_{x_1}(n) - \phi_{x_2}(n) \tag{13}$$

The synchronization coefficient, which quantifies the degree of synchronization between two signals, can be expressed as:

$$Sync = \frac{1}{N}\left|\sum\nolimits_{n=1}^{N} e^{i\cdot\Delta\phi(n)}\right| \tag{14}$$

where N is the length of the time series. The synchronization coefficient ranges from 0 to 100%, with 0% representing complete asynchrony and 100% indicating perfect synchronization.

3.2 Complete synchronization in the MCC neuron

In the MCC neuron model, when we set the external excitation currents are set to $(I_1, I_2) = (0.03, 0.03)$, the membrane potentials of neurons C_1 and C_2 completely overlap, as shown in Fig. 6. By calculating the difference in

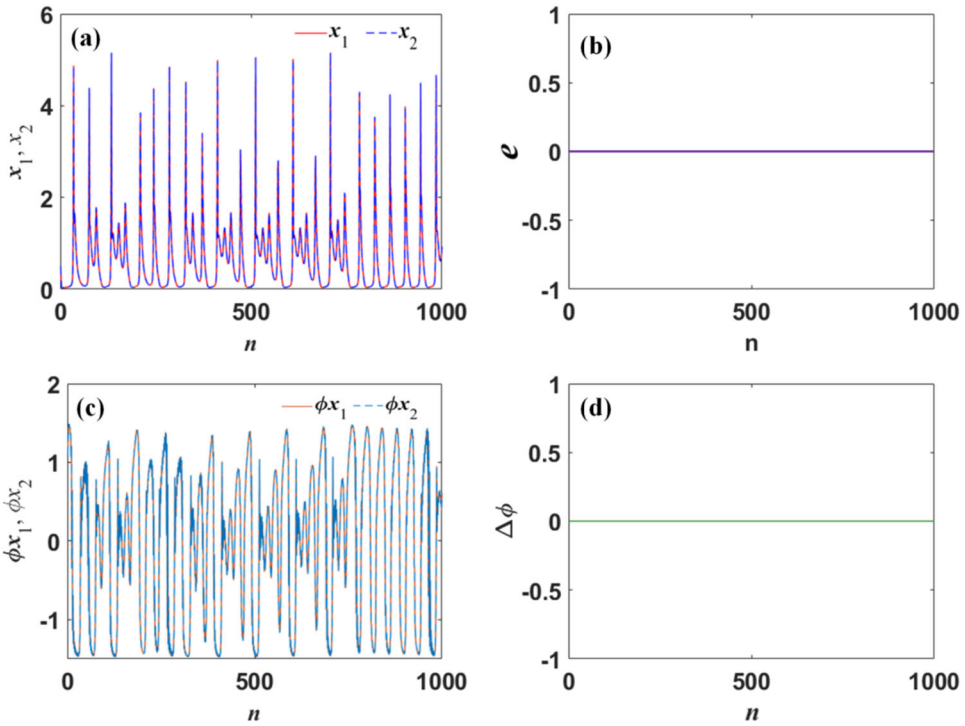


Fig. 6 Complete synchronization discharge of the MCC neuron with external currents $(I_1, I_2) = (0.03, 0.03)$: **a** membrane potential iteration diagram of C_1 and C_2. (**b**) membrane potential difference between C_1 and C_2. (**c**) phase diagram of the membrane potentials of C_1 and C_2. (**d**) phase difference between the membrane potentials of C_1 and C_2. Other parameters and initial conditions: $a = 0.89$, $b = 0.18$, $c = 0.28$, $k = 0.17$, and $(x_1(0), y_1(0), \varphi(0), x_2(0), y_2(0)) = (0.5, 0.1, 0.1, 0.5, 0.1)$

membrane potentials, $e = x_1 - x_2$, we observe that the error e remains zero throughout the entire simulation. The phase orbits and phase difference between the two neurons also coincide perfectly, indicating that neurons C_1 and C_2 are in a state of complete synchronization. The calculated synchronization coefficient is 100%, demonstrating perfect synchronization.

3.3 Phase synchronization analysis in the MCC neuron

In the MCC neuron model, when the external stimulation currents are set to $(I_1, I_2) = (0.03, 0.02)$, we observe that the firing frequencies of neurons C_1 and C_2 are almost identical. As shown in Fig. 7, their phase orbits are nearly overlapping, and the calculated phase difference oscillates around zero. This indicates that the two neurons are in a state of phase synchronization, with the calculated synchronization coefficient being 99.98%, suggesting near-perfect phase synchronization [32].

3.4 Transient synchronization in the MCC neuron

When the external stimulation currents are set to $(I_1, I_2) = (0.03, 0.0301)$, we observe transient synchronization behavior. As shown in Fig. 8a1, the membrane potentials of neurons C_1 and C_2 exhibit different patterns in the iteration ranges of 0–4000 and 5000–10000. The system transitions from a transient state to a stable phase synchronization state after 4000 iterations, with one brief period of perturbation.

Figure 8b1–b3 illustrate the transient phase during the initial 0–4000 iterations. The membrane potential differences between neurons C_1 and C_2 exhibit errors, with nearly opposite firing patterns. During this state, the phase spectrum of C_1 and C_2 shows significant discrepancies, and the phase difference oscillates over a wide range.

As the system self-regulates after 4000 iterations, synchronization gradually occurs, as shown in Fig. 8c1–c3. The membrane potentials of neurons C_1 and C_2 synchronize, their phase spectra converge, and the phase difference approaches zero.

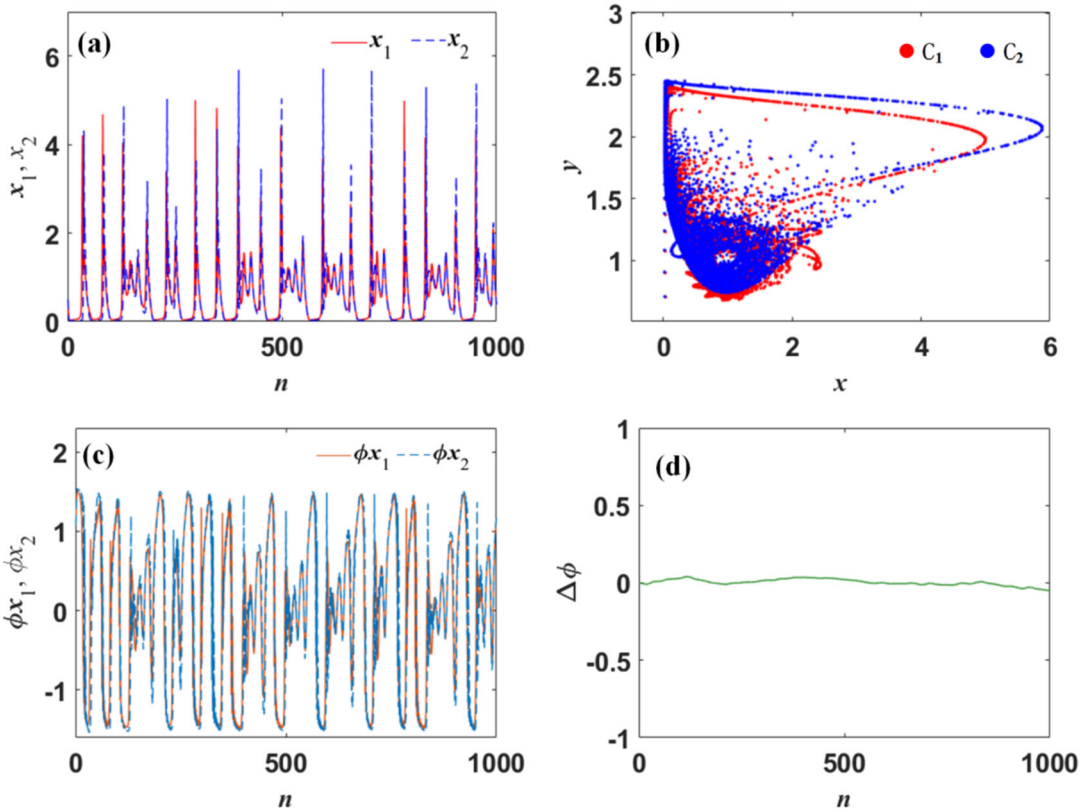


Fig. 7 Phase synchronization discharge of the MCC neuron with external currents $(I_1, I_2) = (0.03, 0.02)$: **a** membrane potential iteration diagram of C_1 and C_2. **b** Phase orbits of C_1 and C_2. **c** Phase diagram of the membrane potentials of C_1 and C_2. **d** Phase difference between the membrane potentials of C_1 and C_2. Other parameters and initial conditions are same as in Fig. 6

4 Offset Boosting and Amplitude Control in the MCC Neuron

4.1 Offset boosting in the MCC neuron

The dynamic behavior of the system can be altered through offset boosting and amplitude control in chaotic maps. In this section, we explore strategies to achieve these modifications using memristor coupling. By adjusting the memristor's offset boosting and amplitude control parameters, we can precisely control the map's dynamic behavior while preserving the fundamental characteristics of the MCC neuron. Our experimental results demonstrate that fine-tuning the memristor parameters enables effective manipulation of neural activity, offering broad applications in neural function simulation and adaptable neural network design.

Consider a modification to the original MCC neuron, where we modify the memristor variable $\varphi(n)$ by adding an offset d, the single parameter d (where d is an arbitrary constant) in the tanh terms inducing the revise of offset [33]. In this way, we can modify the MCC neuron into an offset-adjustable system:

$$\begin{cases} x_1(n+1) = x_1^2(n)e^{(y_1(n)-x_1(n))} + I_1 + k(x_1(n) - x_2(n))\tanh(\varphi(n)+d) \\ y_1(n+1) = ay_1(n) - bx_1(n) + c \\ \varphi(n+1) = \varphi(n) - 0.1(x_1(n) - x_2(n)) \\ x_2(n+1) = x_2^2(n)e^{(y_2(n)-x_2(n))} + I_2 + k(x_2(n) - x_1(n))\tanh(\varphi(n)+d) \\ y_2(n+1) = ay_2(n) - bx_2(n) + c \end{cases} \tag{15}$$

where variable $\varphi(n)$ can now be shifted by a compensating factor. By tuning the parameter d, we can dynamically modulate the behavior of φ, as shown in Fig. 9a. Through offset booster, the variable φ can be shifted to the desired position. Figure 9c, d display the Lyapunov exponents and bifurcation diagram of the system under varying values of d. The bifurcation diagram and Lyapunov exponents indicate that a hyper-chaotic state is maintained by the

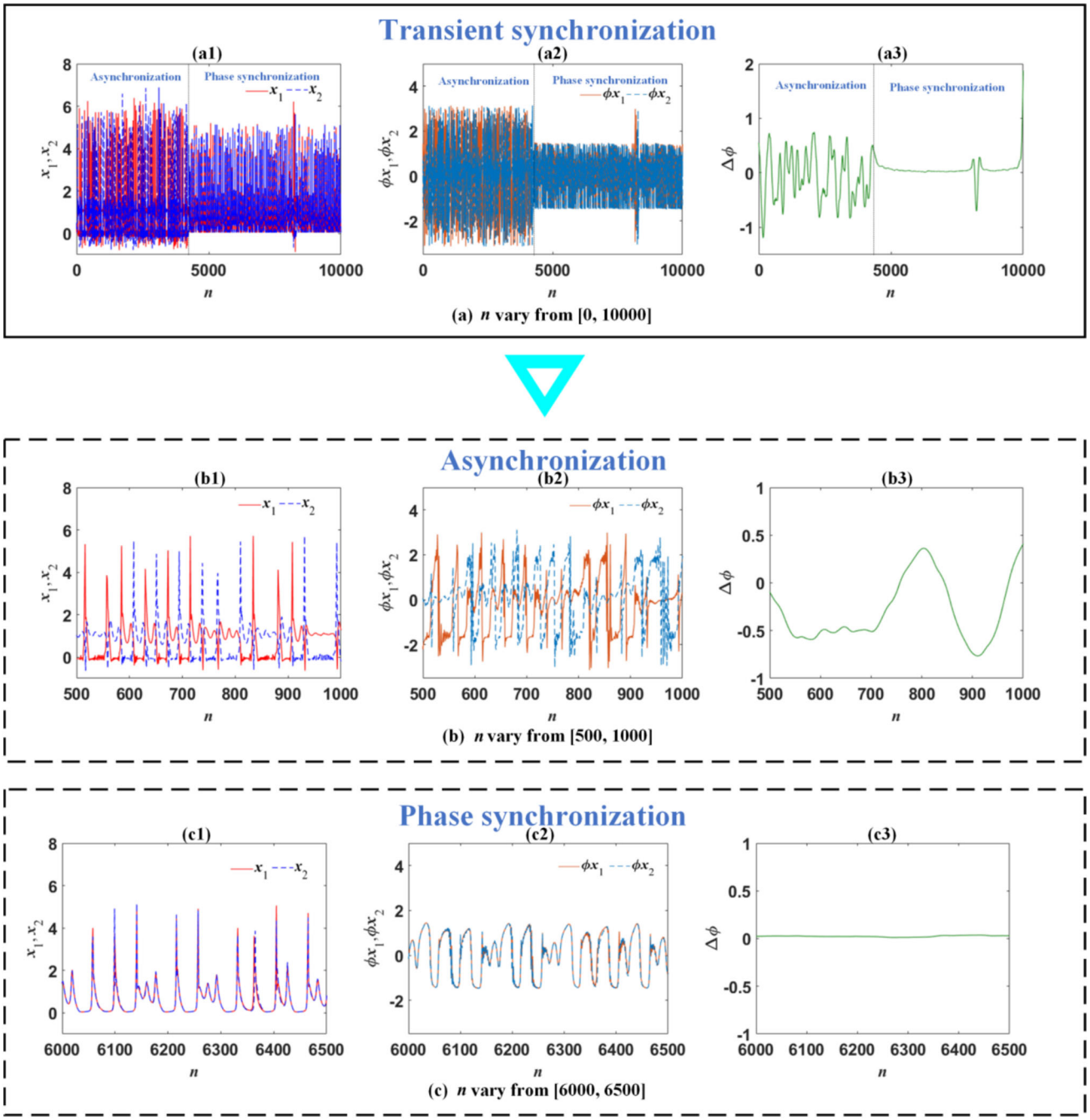


Fig. 8 Transient synchronization discharge of the MCC neuron with external currents $(I_1, I_2) = (0.03, 0.0301)$: **a1**–**c1** membrane potential iteration diagram of C_1 and C_2. **a2**–**c2** phase diagrams of the membrane potentials of C_1 and C_2. **a3**-–**c3** phase differences between the membrane potentials of C_1 and C_2. Other parameters and initial conditions are same as in Fig. 6

system regardless of changes in d. The variable φ in Fig. 9b shows that offset boosting is effective in correcting the average value of the phase orbits and in modulating the average values of the oscillations.

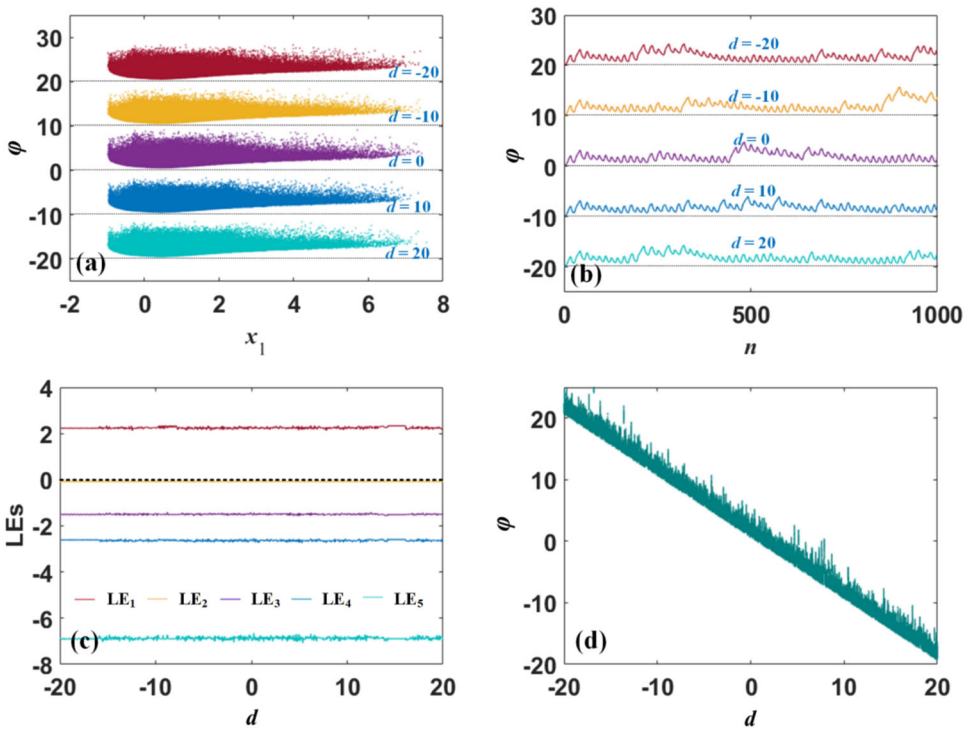


Fig. 9 Offset boosting in the modified MCC neuron (as described in Eq. 15) with $a = 0.89$, $b = 0.18$, $c = 0.28$, $k = 0.25$, under initial conditions $(x_1(0), y_1(0), \varphi(0), x_2(0), y_2(0)) = (0.5, 0.1, 0.1, 0.5, 0.1)$ and external currents $(I_1, I_2) = (0.03, 0.3)$: **a** phase orbits. **b** Discrete sequences. **c** Lyapunov exponents. **d** Bifurcation diagram

4.2 Local amplitude control in the MCC neuron

Another modification to MCC neuron can be realized by adjusting the term $0.1(x_1(n)\text{-}x_2(n))$ to $0.1\ m(x_1(n)\text{-}x_2(n))$, where m is a scaling parameter [34]. The modified mapping can be expressed as:

$$\begin{cases} x_1(n+1) = x_1^2(n)e^{(y_1(n)-x_1(n))} + I_1 + k(x_1(n) - x_2(n))\tanh(\varphi(n)) \\ y_1(n+1) = ay_1(n) - bx_1(n) + c \\ \varphi(n+1) = \varphi(n) - 0.1m(x_1(n) - x_2(n)) \\ x_2(n+1) = x_2^2(n)e^{(y_2(n)-x_2(n))} + I_2 + k(x_2(n) - x_1(n))\tanh(\varphi(n)) \\ y_2(n+1) = ay_2(n) - bx_2(n) + c \end{cases} \tag{16}$$

By adjusting the parameter m, it is observed that changes in m can control the amplitude of the variable φ. As m increases, the range of the state variable φ expands accordingly, as shown in Fig. 10a. When m is varied within the range [1, 40], the mean amplitude of φ enlarges with increasing m, while the range of the membrane potential x_1 remains unchanged. This indicates that the parameter m specifically modulates the amplitude of φ without affecting the neurons' membrane potential. The Lyapunov exponents are shown in Fig. 10c, and the bifurcation diagram is illustrated in Fig. 10d. As the value of m increases, the chaotic range of the system is also expanded.

5 Digital implementation bases on the platform of RISC-V

The circuit implementation of the MCC neuron offers a new means for practical applications, including neuromorphic computing, bionic circuits, and information processing in brain-inspired networks. In most current studies, analog circuits are used to simulate the firing dynamics of biological neurons. However, analog circuits suffer from poor confidentiality, lack of interference resistance, and unstable signals. The CH32-based digital circuit, with its ease of integration, resistance to noise interference, and flexible parameter adjustments for chaotic maps, provides one of the most effective ways to simulate neuronal activities.

The chaotic maps and outputs are computed and processed by the CH32 V307 microcontroller, which is based on the 32-bit RISC-V instruction set and architecture. The microcontroller has a maximum clock frequency of 144 MHz, 256 KB of Flash memory, and 64 KB of SRAM, supporting hardware floating-point operations to significantly improve floating-point computation speed. This processing speed is sufficient to implement the chaotic map. Additionally, the CH32 V307 microcontroller is equipped with two sets of 12-bit digital-to-analog converters

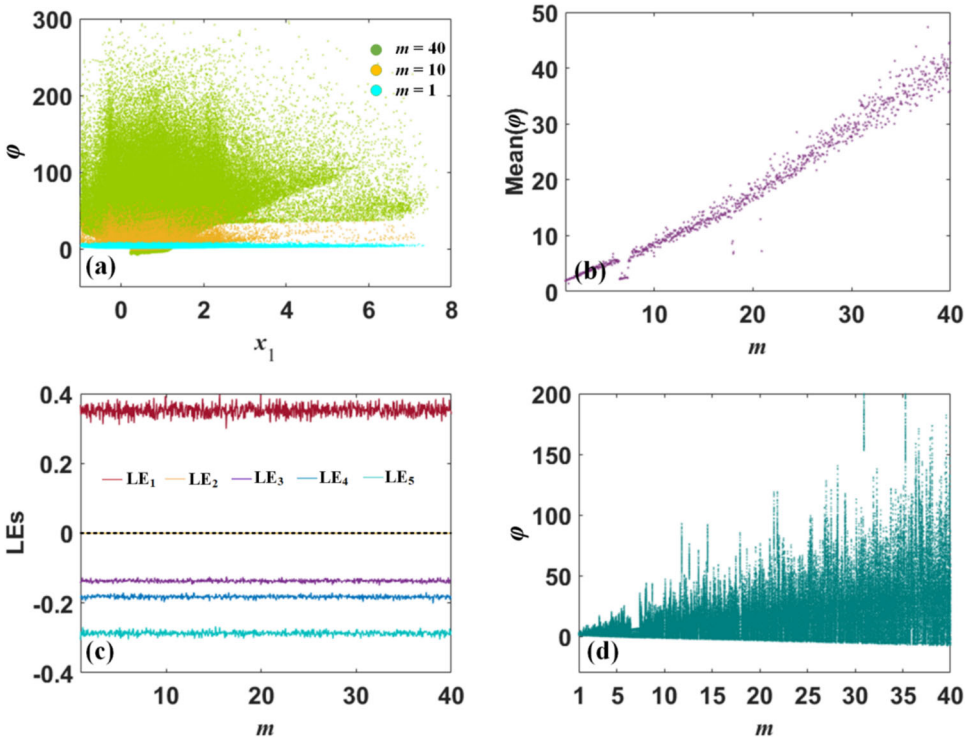


Fig. 10 Local Amplitude Control in the in the modified MCC neuron (as described in Eq. 16) with same parameters and initial conditions as in Fig. 9: **a** phase orbits. **b** Discrete sequences. **c** Lyapunov exponents. **d** Bifurcation diagram

(DACs), enabling the conversion of chaotic digital signals into analog voltage outputs, which can then be observed on an oscilloscope. The circuit implementation process is illustrated in Fig. 11.

The chaotic maps are written into the main program loop, and after initializing the variables and setting the number of iterations, the mapping begins. For each iteration, the chaotic data is linearly mapped to a value between 0 and 4095, and this data is written to the DAC-DORx register to start the DAC conversion process, which converts the chaotic digital signal into the initial value for the next iteration until the set number of iterations is reached. The outputs of the two sets of analog voltage signals are transmitted to the signal input terminals of the oscilloscope. The CH32-based digital circuit platform is shown in Fig. 12.

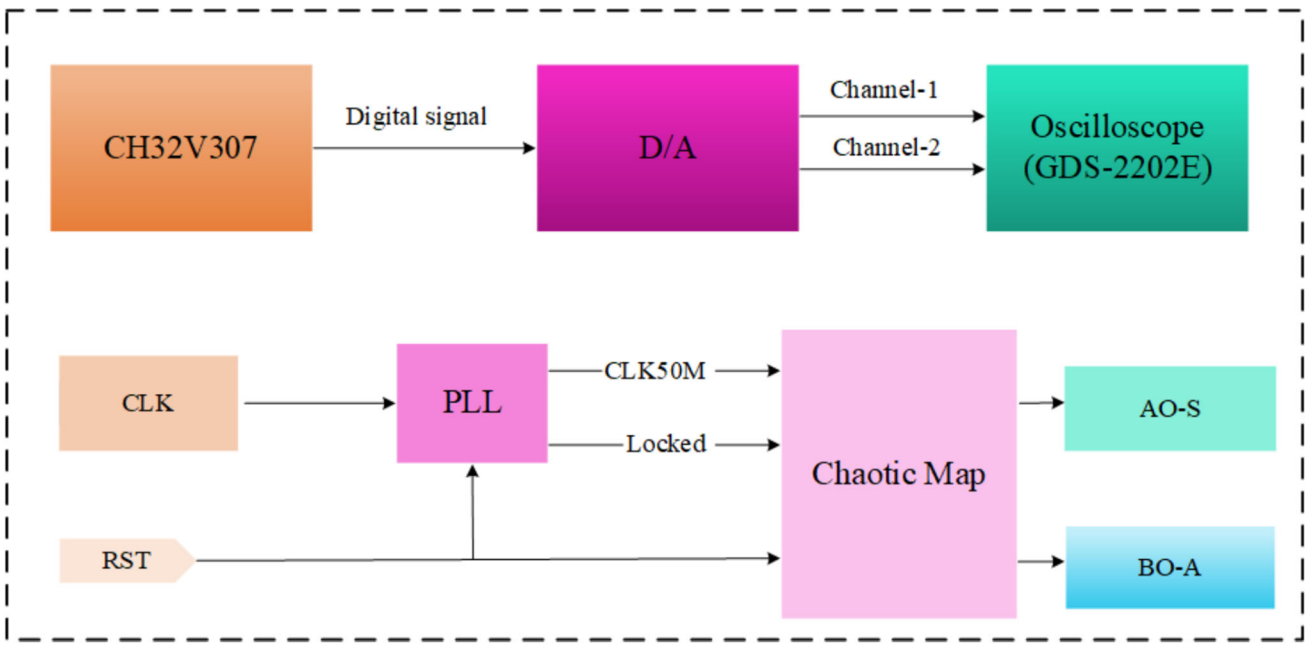


Fig. 11 Schematic of the CH32-based circuit implementation

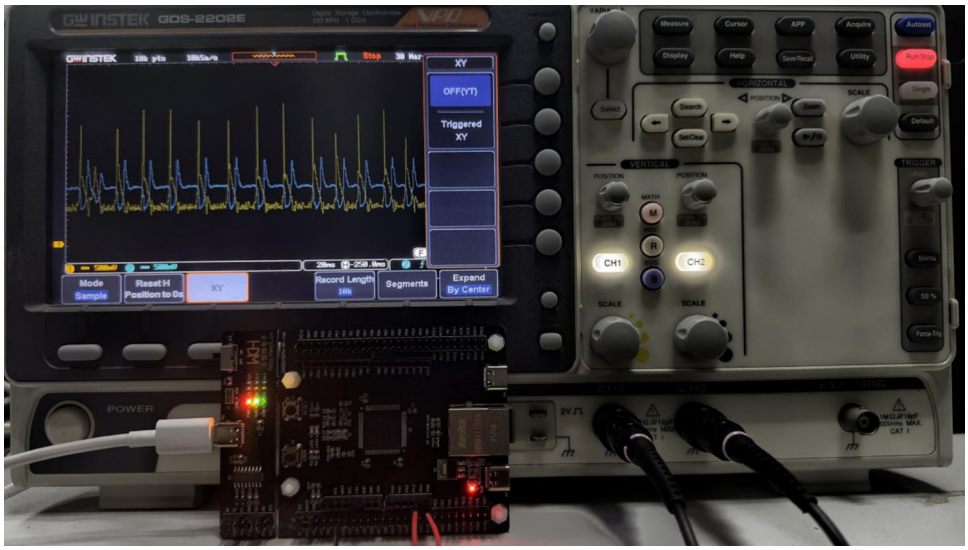


Fig. 12 Platform of CH32-based digital circuit

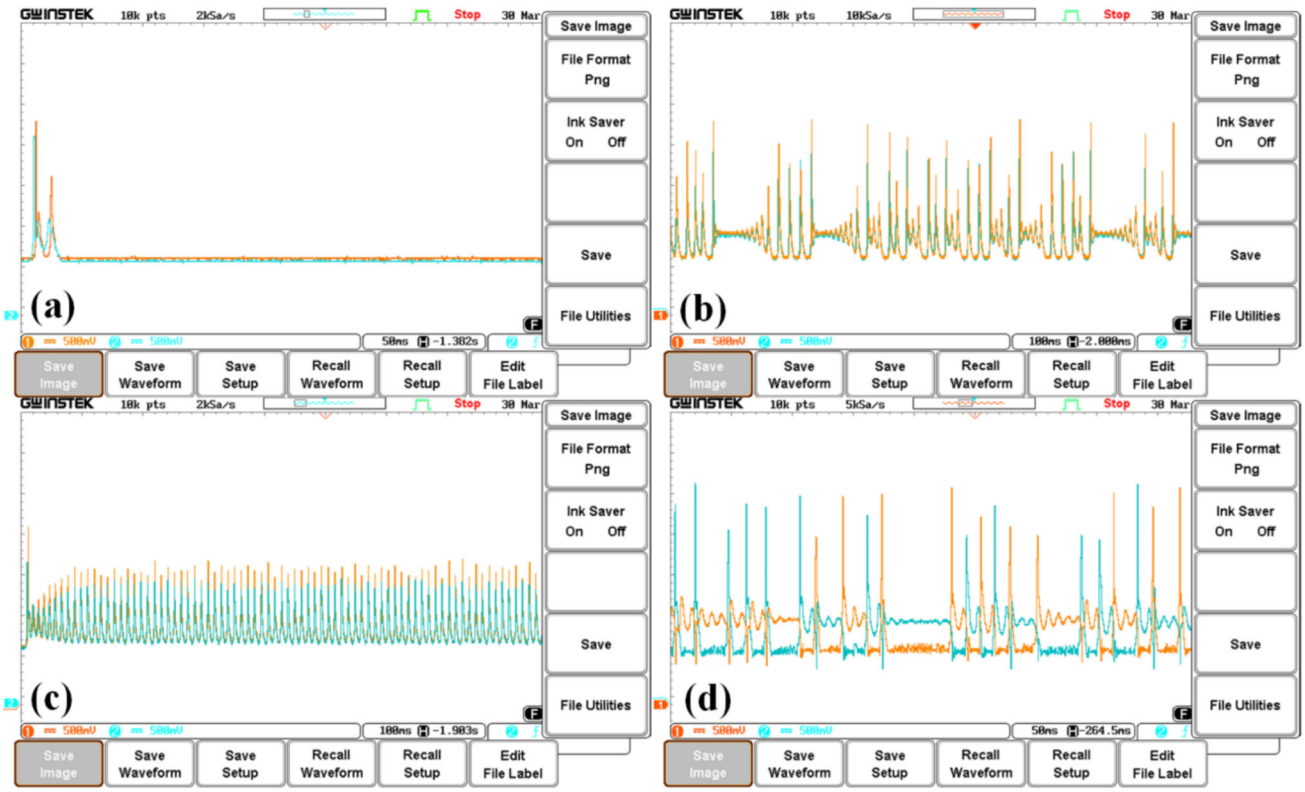


Fig. 13 Typical oscillations of the original MCC neuron (Eq. 2) implemented in the CH32-based circuit. **a** Quiescent neurons with $(I_1, I_2) = (0.03, -0.02)$, **b** spiking and bursting neurons with $(I_1, I_2) = (0.05, 0.01)$, **c** bursting and spiking neurons with $(I_1, I_2) = (0.05, 0.04)$, and **d** reverse spiking and bursting neurons with $(I_1, I_2) = (0.041, 0.04)$. Other parameters and initial conditions: $a = 0.89$, $b = 0.18$, $c = 0.28$, $k = 0.17$, and $(x_1(0), y_1(0), \varphi(0), x_2(0), y_2(0)) = (0.5, 0.1, 0.1, 0.5, 0.1)$

In Fig. 13, we present the membrane potential waveforms of neurons C_1 and C_2 under four different firing states, as simulated on the CH32 digital circuit platform with varying external stimuli. Figure 14 shows how the synchronization state of the MCC neuron changes under external excitation current adjustment. Figure 15 illustrates the system's behavior after adjusting offset booster and amplitude control key, demonstrating the adaptability of the MCC neuron to different memristor parameters. These experimental results are in line with the computational results as explored in previous sections, verifying the corresponding theoretical analysis.

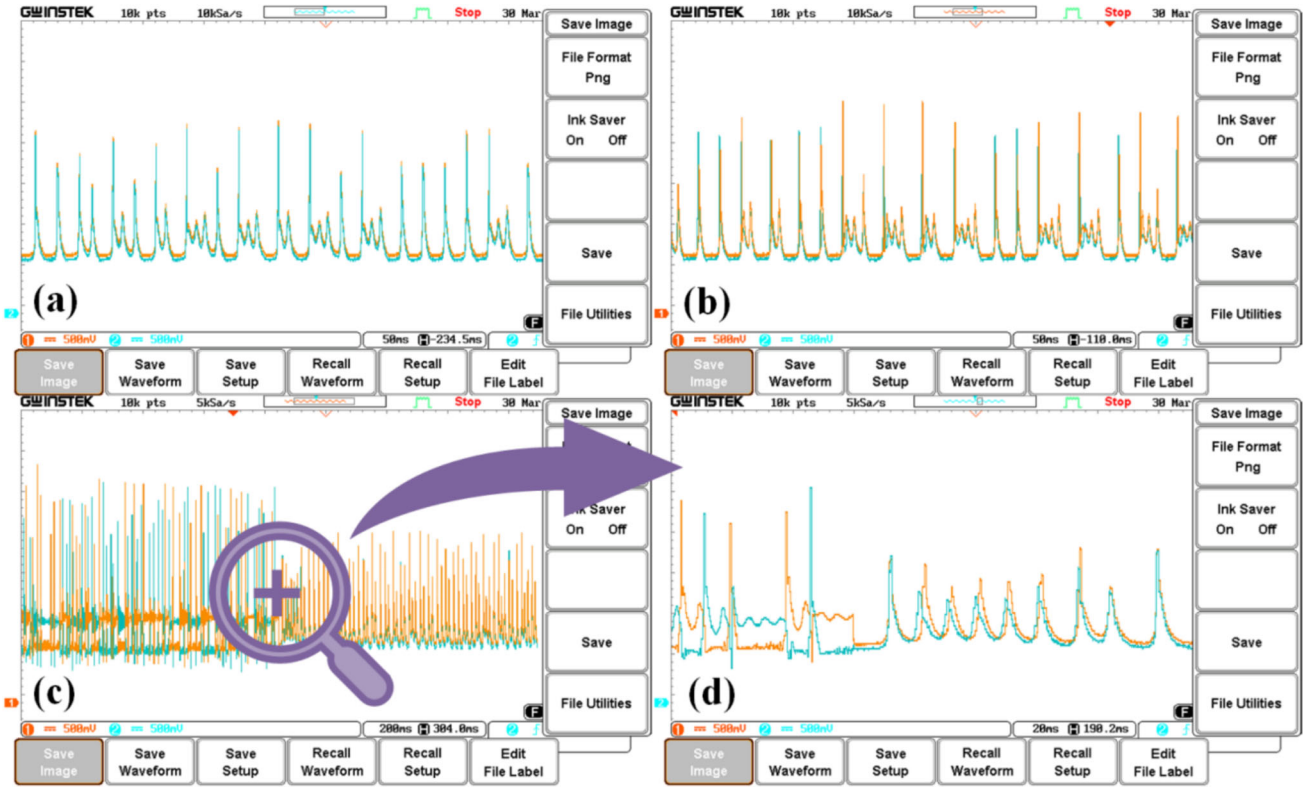


Fig. 14 Synchronization discharge of the MCC neuron implemented in the CH32-based circuit. **a** Complete Synchronization with $(I_1, I_2) = (0.03, 0.03)$. **b** Phase Synchronization with $(I_1, I_2) = (0.03, 0.02)$. **c**, **d** Transient Synchronization with $(I_1, I_2) = (0.03, 0.0301)$. Other parameters and initial conditions are the same as in Fig. 13

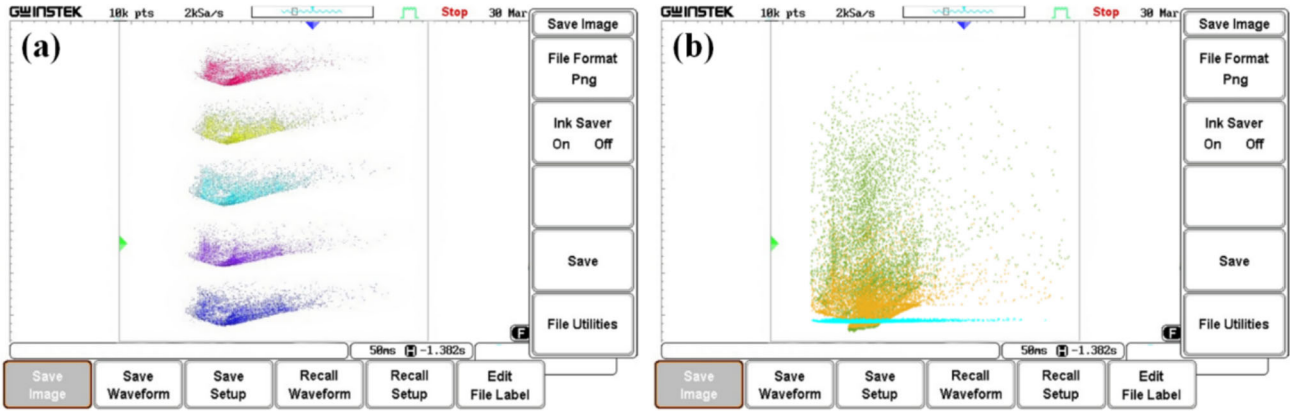


Fig. 15 Offset boosting and local amplitude control of the modified MCC neurons (Eqs.15 and 16), with external currents $(I_1, I_2) = (0.03, 0.3)$: **a** offset boosting. **b**) local amplitude control. Other parameters and initial conditions: $a = 0.89$, $b = 0.18$, $c = 0.28$, $k = 0.25$, and $(x_1(0), y_1(0), \varphi(0), x_2(0), y_2(0)) = (0.5, 0.1, 0.1, 0.5, 0.1)$

6 Conclusion

In this paper, we propose a tanh-type memristor-coupled Chialvo (MCC) neuron model capable of achieving controllable synchronization states. The synchronization processes are analyzed using the Hilbert transform, while Lyapunov exponents and bifurcation diagrams reveal the system's complex dynamic behaviors. By adjusting the external excitation currents, various synchronization states are successfully generated. Additionally, the mechanisms of offset boosting and local amplitude control further enhance the system's application potential. Numerical

simulations and theoretical analyses are conducted on a circuit platform implemented with the CH32 microcontroller. The chaotic firing behaviors observed in the MCC neuron demonstrate broad applicability in fields such as random number generation, cryptography, signal processing, and optimization through random walks. Consequently, the MCC neuron model, with its synchronization effects, not only opens new avenues for optimization in these areas but also provides valuable insights into the synchronization mechanisms of biological electrical signals.

Acknowledgements This work was supported financially by The University Synergy Innovation Program of Anhui Province under Grant GXXT-2023-012. DRC thanks HKBU for funding his Distinguished Professorship during these studies.

Author contributions

Lili Wang: Investigation, Data curation, and Writing-original draft. Hao Gao: Circuit implementation, Methodology, Mathematical analysis. Chunbiao Li: Validation and Circuit implementation. Qianyuan Tang: Conceptualization, Writing—review & editing Dante Chialvo: Conceptualization, Writing—review & editing.

Data availability The authors confirm that all relevant data are within the paper.

Declarations

Conflict of interest The authors have no conflicts to disclose.

References

1. M.J. Ison, R. Quian Quiroga, I. Fried, Rapid encoding of new memories by individual neurons in the human brain. Neuron **87**, 220–230 (2015)
2. C. Mead, Neuromorphic electronic systems. Proc. IEEE **78**, 1629–1636 (1990)
3. H. Lin, C. Wang, L. Cui, Y. Sun, C. Xu, F. Yu, Brain-like initial-boosted hyperchaos and application in biomedical image encryption. IEEE Trans. Ind. Inform. **18**, 8839–8850 (2022)
4. S. Gepshtein, A.S. Pawar, S. Kwon, S. Savelev, T.D. Albright, Spatially distributed computation in cortical circuits. Sci. Adv. **8**, eabl5865 (2022)
5. X. Ge, C. Li, Y. Li, C. Zhang, C. Tao, Multiple alternatives of offset boosting in a symmetric hyperchaotic map. Symmetry **15**, 712 (2023)
6. C. Li, C. Yi, Y. Li, S. Mitro, Z. Wang, Offset boosting in a discrete system. Chaos Interdiscip. J. Nonlinear Sci. **34**, 031102 (2024)
7. P. Fries, A mechanism for cognitive dynamics: neuronal communication through neuronal coherence. Trends Cogn. Sci. **9**, 474–480 (2005)
8. J. Fell, N. Axmacher, The role of phase synchronization in memory processes. Nat. Rev. Neurosci. **12**, 105–118 (2011)
9. F. Varela, J.P. Lachaux, E. Rodriguez, J. Martinerie, The brainweb: phase synchronization and large-scale integration. Nat. Rev. Neurosci. **2**, 229–239 (2001)
10. G. Buzsáki, A. Draguhn, Neuronal oscillations in cortical networks. Science **304**, 1926–1929 (2004)
11. J.J. Hopfield, Neural networks and physical systems with emergent collective computational abilities. Proc. Natl. Acad. Sci. **79**, 2554–2558 (1982)
12. K. Fukushima, Neocognitron: a self-organizing neural network model for a mechanism of pattern recognition unaffected by shift in position. Biol. Cybern. **36**, 193–202 (1980)
13. J. Ma, S. Li, D. Zhou, Mapping biological neuron dynamics into an interpretable two-layer artificial neural network (2023). https://doi.org/10.48550/arXiv.2305.12471
14. D.R. Chialvo, Generic excitable dynamics on a two-dimensional map. Chaos Solitons Fractals **5**, 461–479 (1995)
15. D.R. Chialvo, Emergent complex neural dynamics. Nat. Phys. **6**, 744–750 (2010)
16. H. Bao, A. Hu, W. Liu, B. Bao, Hidden bursting firings and bifurcation mechanisms in memristive neuron model with threshold electromagnetic induction. IEEE Trans. Neural Netw. Learn. Syst. **31**, 502–511 (2020)
17. L. Chua, Memristor—the missing circuit element. IEEE Trans. Circuit Theory **18**, 507–519 (1971)
18. S. He, J. Liu, H. Wang, K. Sun, A discrete memristive neural network and its application for character recognition. Neurocomputing **523**, 1–8 (2023)
19. C. Shang, S. He, K. Rajagopal, H. Wang, K. Sun, Dynamics and chimera state in a neural network with discrete memristor coupling. Eur. Phys. J. Spec. Top. **231**, 4065–4076 (2022)
20. F. Yang, Z. Han, G. Ren, Q. Guo, J. Ma, Enhance controllability of a memristive neuron under magnetic field and circuit approach. Eur. Phys. J. Plus **139**, 534 (2024)
21. X. Zhang, C. Li, H.H.-C. Iu, L. Zhao, Y. Yang, A chaotic memristive Hindmarsh-Rose neuron with hybrid offset boosting. Chaos Solitons Fractals **185**, 115150 (2024)
22. F. Yang, X. Song, J. Ma, A memristive map neuron under noisy electric field. Chin. J. Phys. **91**, 287–298 (2024)

23. F. Yang, J. Ma, F. Wu, Review on memristor application in neural circuit and network. Chaos Solitons Fractals **187**, 115361 (2024)
24. H. Wang, H. Chen, K. Sun, W. Zhu, Z. Yao, Spatiotemporal dynamics and synchronization in a memristive Chialvo neural network. Nonlinear Dyn. (2025). https://doi.org/10.1007/s11071-024-10599-7
25. Y. Li, C. Li, T. Lei, Y. Yang, G. Chen, Offset boosting-entangled complex dynamics in the memristive Rulkov neuron. IEEE Trans. Ind. Electron. **71**, 9569–9579 (2024)
26. Y. Li, C. Li, S. Zhang, G. Chen, Z. Zeng, A self-reproduction hyperchaotic map with compound lattice dynamics. IEEE Trans. Ind. Electron. **69**, 10564–10572 (2022)
27. F. Yang, X. Song, Z. Yu, Adaptive mode selection of electrical activities in a neuron with a memristive ion channel. Nonlinear Dyn. (2024). https://doi.org/10.1007/s11071-024-10710-y
28. C. Li, İ PehliVan, J.C. Sprott, Amplitude-phase control of a novel chaotic attractor. Turk. J. Electr. Eng. Comput. Sci. **24**, 1–11 (2016)
29. G. Vivekanandhan, H. Natiq, Y. Merrikhi, K. Rajagopal, S. Jafari, Dynamical analysis and synchronization of a new memristive Chialvo neuron model. Electronics **12**, 545 (2023)
30. S. S. Muni, H. O. Fatoyinbo, I. Ghosh, Dynamical effects of electromagnetic flux on Chialvo neuron map: Nodal and network behaviors (2022) https://doi.org/10.48550/arXiv.2201.03219
31. W. Liu, K. Sun, S. He, H. Wang, The parallel chaotification map and its application. IEEE Trans. Circuits Syst. Regul. Pap. **70**, 3689–3698 (2023)
32. J.P. Lachaux, E. Rodriguez, J. Martinerie, F.J. Varela, Measuring phase synchrony in brain signals. Hum. Brain Mapp. **8**, 194–208 (1999)
33. F. Yang, X. Song, Z. Yu, Dynamics of a functional neuron model with double membranes. Chaos Solitons Fractals **188**, 115496 (2024)
34. X. Song, F. Yang, A light-temperature neuron and its adaptive regulation. Phys. Scr. **99**, 125247 (2024)

Springer Nature or its licensor (e.g. a society or other partner) holds exclusive rights to this article under a publishing agreement with the author(s) or other rightsholder(s); author self-archiving of the accepted manuscript version of this article is solely governed by the terms of such publishing agreement and applicable law.